minerals

MDPI

Article

Experimental Modeling of Diamond Resorption during Mantle Metasomatism

Alexander F. Khokhryakov *, Alexey N. Kruk, Alexander G. Sokol and Denis V. Nechaev

V.S. Sobolev Institute of Geology and Mineralogy SB RAS, 630090 Novosibirsk, Russia; krukan@igm.nsc.ru (A.N.K.); sokola@igm.nsc.ru (A.G.S.); nechaev@igm.nsc.ru (D.V.N.)
* Correspondence: khokhr@igm.nsc.ru

Abstract: The morphology of resorbed diamond crystals is a valuable source of information on the composition and ascent rate of kimberlite magmas, as well as on possible redox conditions in protolith. Previously, diamond resorption was thoroughly investigated at P–T–fO_2 parameters of the kimberlite magma ascent. In this study, we investigated diamond resorption using unaltered group I kimberlite and model carbonatite at P–T–fO_2 parameters that are typical of the peridotite source of kimberlite magmas in the subcontinental lithospheric mantle. An analysis of previous studies made it possible to determine the rate of diamond octahedron transformation into a spherical tetrahexahedron depending on the composition of the carbonate–silicate melt. It was shown that the rate of diamond resorption at 6.3 GPa increases in all the investigated systems as fO_2 and temperature rise. There is a steady decrease in the diamond resorption rate as pressure increases from 1 GPa to 6.3 GPa. The morphology comparison of the experimentally produced samples with natural diamonds is indicative of the significant contribution of metasomatic alteration of protolith by the oxidized agent and at the initial stages of kimberlite magma ascent to the resorption of natural diamonds.

Keywords: diamond resorption; kimberlite melts; oxygen fugacity; high-pressure experiment

Citation: Khokhryakov, A.F.; Kruk, A.N.; Sokol, A.G.; Nechaev, D.V. Experimental Modeling of Diamond Resorption during Mantle Metasomatism. *Minerals* **2022**, *12*, 414. https://doi.org/10.3390/min12040414

Academic Editor: Paolo Nimis

Received: 18 February 2022
Accepted: 24 March 2022
Published: 28 March 2022

1. Introduction

In recent years, there have been proponents of the point of view that diamond resorption under mantle conditions is insignificant and occurs through a different process with respect to diamond resorption in a kimberlite melt during its ascent to the Earth's surface [1–5]. The ideal ditrigonal layers on octahedron faces and rounded diamond tetrahexahedroids with glossy surfaces are assumed to be formed during the interaction between the diamond and a COH fluid only during kimberlite ascent. On the contrary, during mantle metasomatism, diamond resorption in the presence of fluids and volatile-rich silicate–carbonate melts occurs only with the formation of deep pits (trigons) and triangular and serrate laminae on the octahedral faces. An important argument in support of this assumption is that most diamonds in mantle xenoliths lack resorption patterns, and no rounded crystals have been found. Diamond resorption from xenoliths is usually insignificant and occurs in the form of triangular pits and ditrigonal layers on octahedron faces. On rare occasions, xenoliths contain diamond crystals with subordinate rounded tetrahexahedroid surfaces at the octahedron edges [6]. However, an investigation of the internal structure of natural diamond crystals using cathodoluminescence showed that the growth of diamonds in some cases was periodically followed by the stage of resorption [5,7,8]. In this case, there is some uncertainty as to how significant these resorption stages are. The discovery of large, rounded diamonds in kimberlites of various diamondiferous provinces indicates that possible intense diamond resorption was occurring for a longer time compared to the time suggested for kimberlite melt ascent from the mantle to the Earth's surface. According to Haggerty [9] and Gurney et al. [10], significant diamond resorption might occur in the subcratonic mantle due to changes in redox conditions and/or during fluid metasomatism.

A number of studies have experimentally modeled diamond dissolution/resorption under high pressure and high temperature conditions; their results are reviewed by Fedortchouk [3] and Palyanov et al. [11]. The modeling of diamond dissolution was performed in kimberlite and alkaline basalt melts with different contents of a H_2O–CO_2 fluid and in various model carbonate, carbonate–silicate, and silicate systems at pressures of 5–7.5 GPa, and temperatures of 1100–1750 °C (Figure 1) [2,12–18]. The presence of water in silicate or carbonate melts was found to be the major factor controlling the formation of diamond tetrahexahedroides, similar to natural rounded diamonds. The curvature of the rounded surfaces of tetrahexahedroids was experimentally shown to be related to the habit of original flat-faced crystals and to be an indicator of the degree of their dissolution [15,19]. The composition of melts and fluids was found to affect the features of diamond resorption [2,16,18,20]. Moreover, Khokhryakov and Palyanov [17] showed a relationship between some elements of the tetrahexahedroid microrelief and the features of the internal crystal structure at a pressure of 5.7 GPa and temperature of 1300 °C. However, it is difficult to correctly compare these data with diamond resorption at low pressures (1–3 GPa) because experimental conditions differ in terms of the number of parameters, in particular, in the system composition and redox conditions.

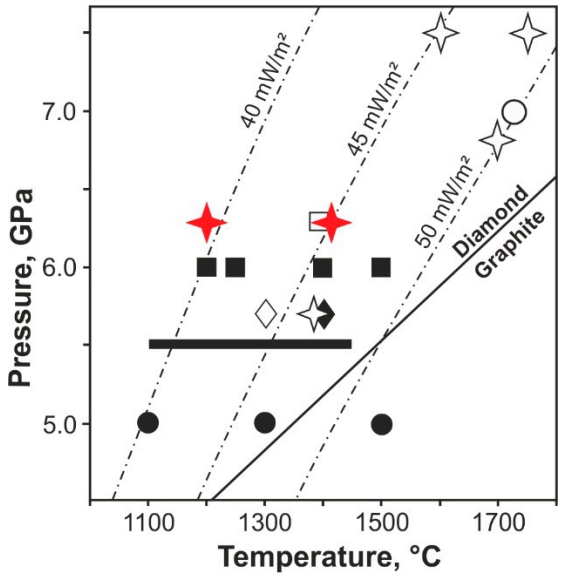

Figure 1. P–T parameters of the experiments on diamond resorption under mantle conditions. Red stars indicate the experiments of this work. Additionally, the conditions of previous experiments are given: an open square—kimberlite–H_2O and carbonatite–H_2O systems [18]; solid squares—the synthetic CaO-MgO-SiO_2-CO_2-H_2O system [2]; open stars—carbonates ± H_2O± CO_2 [16]; an open circle—$CaCO_3$ melt [14]; solid circles—H_2O fluid [12]; an open rhombus—the $CaCO_3$–H_2O systems [17]; a solid rhombus—carbonates–H_2O and diopside–H_2O systems [19]; and bold horizontal bar—the alkaline basalt–H_2O system [13]. Model conductive geotherms are presented according to Pollack and Chapman [21]. The equilibrium line graphite-diamond is presented according to Kennedy and Kennedy [22].

Recently, we have reported the experimental findings on diamond resorption in the carbonatite + H_2O ± CO_2 and kimberlite + H_2O ± CO_2 systems, which modeled the intermediate stage of kimberlite melt ascent to the Earth's surface at 3.0 GPa, T = 1200–1400 °C, and fO_2 in the range from NNO –2 to NNO +3.2 [23]. In this study, we investigated diamond resorption at the same T–fO_2 parameters (Figure 2) and in the same systems, but at higher pressure (6.3 GPa), thereby modeling possible diamond resorption at conditions of the subcontinental lithospheric mantle (hereinafter referred to as, SLM) base, at depths of about 200 km. Our new findings made it possible to compare the resorption patterns and rates depending on pressure and, therefore, reveal the characteristic features of diamond

resorption by metasomatic agents at the base of CLM, and by a kimberlite melt at the initial stage of its ascent to the Earth's surface.

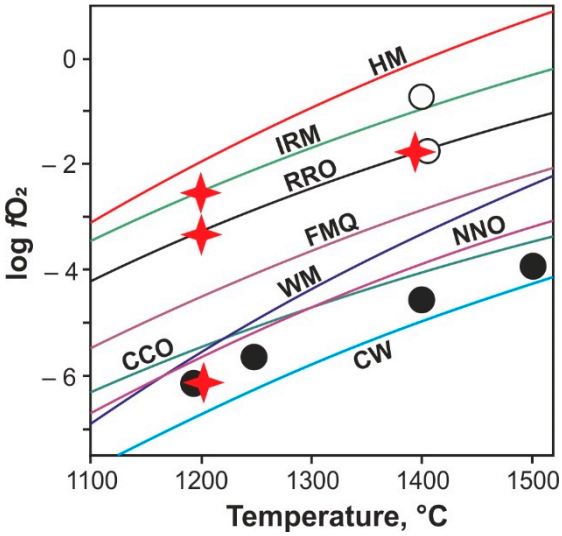

Figure 2. Redox conditions of the experimental runs on diamond resorption at a pressure of 6.3 GPa. Red stars indicate the experiments of this work. The positions of the buffers, CCO and CW are given according to the following data: FMQ (fayalite–magnetite–quartz) and NNO (Ni-NiO) by Ballhaus et al. [24]; RRO (Re-ReO2) by Campbell et al. [25]; CW—water maximum by Foley [26]; HM (magnetite–hematite) and WM (wüstite–magnetite) by Kadik and Lukanin [27]; CCO—buffer equilibria by Frost and Wood [28]; IRM (ilmenite–rutile–magnetite) according to our data, see details in [29]. In addition, the conditions of previous experiments are given, in which the oxygen fugacity in the samples was controlled: open circles—the kimberlite–H_2O and carbonatite–H_2O systems at 6.3 GPa [18]; solid circles—the synthetic CaO-MgO-SiO_2-CO_2-H_2O system at 6.0 GPa [2].

2. Materials and Methods

2.1. Starting Compositions

We used the same starting compositions as in our previous study on diamond dissolution at a pressure of 3 GPa [23]: fresh kimberlites from the Udachnaya–East pipe (Yakutia) (hereinafter referred to as Ud) modeling kimberlite-like melts, and a model multicomponent composition modeling carbonatite melts genetically related to subduction zones [30] (hereinafter, GS). The procedure for preparing kimberlite for experiments was described by Sokol et al. [31]. The GS composition was prepared from carbonates ($MgCO_3$, $CaCO_3$, Na_2CO_3, and K_2CO_3) and oxides (MgO, SiO_2, Al_2O_3, Cr_2O_3, TiO_2, FeO, Fe_2O_3, MnO, and NiO) with 99.9% purity and natural olivine from the xenolith of the Udachnaya–East pipe containing 9 wt% FeO. Distilled water or anhydrous oxalic acid ($C_2H_2O_4$, hereinafter, OA) (10 wt%) was also added to the original mixture. Earlier in [32], based on thermodynamic calculations and gas chromatography data of the quenched fluid, it was shown that the decomposition products of anhydrous oxalic acid ($C_2H_2O_4$) at 5.7 GPa and 1200–1420 °C were dominated by CO_2 and H_2O; minor amounts of CO (<2.6 mol.%), CH_4 and H_2 (<0.1 mol.%) were also present. Given the low concentration of CO in products, anhydrous oxalic acid was decomposed as follows: $2H_2C_2O_4 \rightarrow 3CO_2 + 2H_2O + C^0$. This reaction is supported by the detection of graphite flakes in the experiments where no diamond resorption occurred (e.g., in experimental run no. 1753_1). Thus, under experimental conditions, OA is decomposed into 73 wt% CO_2, 20 wt% H_2O, and 7 wt% C. The compositions of the initial mixtures used in the experiments are given in Table 1.

Table 1. Initial compositions of the systems used in the experiments on diamond resorption.

	GS-H_2O	GS-OA	Ud-H_2O	Ud-OA
SiO_2	0.56	0.57	25.03	25.19
TiO_2	0.02	0.02	1.23	1.24
Al_2O_3	0.66	0.67	2.67	2.68
Cr_2O_3	-	-	0.11	0.11
Fe_2O_3	-	-	2.82	2.84
FeO	3.61	3.63	4.58	4.61
MnO	-	-	0.14	0.14
NiO	-	-	0.19	0.19
MgO	4.34	4.36	25.18	25.33
CaO	14.25	14.34	12.12	12.19
Na_2O	0.16	0.16	2.33	2.34
K_2O	28.45	28.64	1.67	1.68
H_2O	9.09	1.83	11.36	4.11
P_2O_5	-	-	0.37	0.38
CO_2	38.85	45.78	8.58	15.34
S	-	-	0.30	0.30
F	-	-	0.13	0.13
Cl	-	-	1.20	1.21
Total	99.99	100.00	100	100

Natural diamond crystals from kimberlites of Yakutia (Russia), 0.6–0.7 mm in size and weighing 0.24–0.40 mg, were used for dissolution. Octahedral crystals with flat faces or with trigonal layers on the faces were selected for the experiments. The crystals were colorless, without any inclusions or cracks visible under an optical microscope, and without any signs of natural resorption. Before and after each experiment, diamond crystals were cleaned in a mixture of concentrated sulfuric acid and an aqueous solution of potassium permanganate. After each acid treatment, diamonds were washed by boiling in distilled water.

Diamond crystals were studied by optical microscopy using a Carl Zeiss Axio Imager Z2m microscope. Differential interference contrast (DIC) was used to enhance the contrast of the face relief image. Total interference contrast (TIC) was used to measure the inclination angles of etching pit walls. Crystals were weighed with an accuracy of ±0.01 mg before and after the experiments. The resorption rate was calculated as $(mg/mm^2 \times min^{-1}) \times 10^3$ to avoid the influence of the size of diamond crystals on their resorption rate. The surface area of the crystals was determined from their mass, diamond density, and their octahedral shape. The error in calculating the rates of diamond resorption was no more than $\pm 0.025\ mg/mm^2 \times min^{-1} \times 10^3$. This estimate takes into account the accuracy of weighing, and the uncertainty related to the surface area of the resorbed crystals.

To control fO_2 with the Re–ReO_2 (RRO) buffer in the experiments at 1200 °C and 1400 °C (Figure 3a), we applied the methodological approach used in [18]. The starting material (50 mg) and two diamond crystals were placed into Pt capsules (outer diameter, 5 mm; wall thickness, 0.2 mm) lined on the inside with Re foil. After sealing, the Pt capsules were placed into a container consisting of a mixture of Fe_2O_3 and CsCl. Because the external Fe_2O_3-bearing container provided very low fH_2 around the Pt capsule, hydrogen outflow arose from the sample, and the oxidation of Re to ReO_2 took place. This approach provided control over fO_2 in the capsule in the Re–ReO_2 (RRO) buffer [18]. In addition, the Re lining of Pt capsules minimized iron loss from the samples. To control fO_2 using the ilmenite–rutile–magnetite (IRM) buffer in the experiments at 1200 °C (Figure 3b), we used Au capsules with an outer diameter of 2 mm and wall thickness of 0.2 mm. The starting material (11 mg) and one diamond crystal were placed into capsules. The capsules were hermetically sealed by arc welding after assembly.

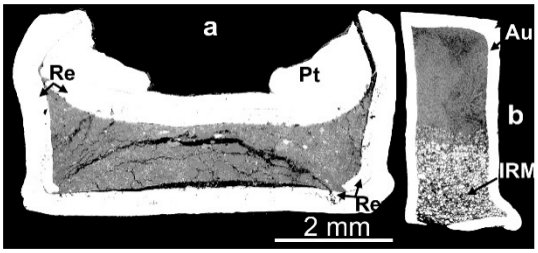

Figure 3. Micrographs of the capsules after the experiments. (**a**) A Pt ampoule with Re lining (run no. 1666_3_3, Ud-H2O system); (**b**) Au ampoule with internal IRM buffer (run no. 2223_2_3, Ud-OA system).

Platinum capsules lined with Re foil were used in the experiments carried out at 1200 °C without internal or external buffer fO_2. The capsules had an outer diameter of 5 mm and wall thickness of 0.2 mm. Such capsules contained the starting material (50 mg) and two diamond crystals. Rhenium was not oxidized in these experiments, and therefore fO_2 was not buffered in it. Redox conditions in these experiments were set based on the data on the composition of carbon-saturated H_2O–CO_2 fluids obtained using a similar high-pressure cell in the unbuffered experiments at 5.7 GPa and 1420 °C [32]. The composition of carbon-saturated fluid in a Pt capsule (80 mol.% H_2O + 20 mol% CO_2) allows one to estimate fO_2 in the samples produced at 6.3 GPa and 1200 °C in the range between CCO and the carbon-saturated water maximum (CW) [26]. Values corresponding to half of the CCO–CW interval match fO_2 of NNO-0.5 at these P–T parameters (Figure 2).

2.2. High-pressure Apparatus and Analytical Techniques

Experiments at 6.3 GPa were carried out in a split-sphere multi-anvil high-pressure apparatus [33]. A high-pressure cell was sized 21.1 × 21.1 × 25.4 mm, and graphite heaters had an inner diameter of 12.2 mm and a height of 18.8 mm. Pressure was calibrated by recording changes in the resistance of Bi at 2.55 GPa and PbSe at 4.0 and 6.8 GPa at room temperature, and at 1350 °C by bracketing the graphite–diamond equilibrium in the $Ni_{0.7}$–$Fe_{0.3}$–C system [34]. The temperature was monitored in each experimental run with a PtRh6/PtRh30 thermocouple calibrated at 6.3 GPa using the melting points of Al and Ag [35]. Pressure and temperature were measured with an accuracy of ±0.1 GPa and ±20 °C, respectively [33,35]. The temperature pattern within the low-gradient zone of the high-pressure cell at 1200 °C and 1350 °C was estimated by Sokol et al. [36] via simulation using the software elaborated on by Hernlund et al. [37]. At the end of an experimental run, the samples were quenched at 150 °C/s under isobaric conditions.

After the experiment, the capsule with a sample was cleaned from CsCl, dried, and weighed to control the tightness of the capsule. After extracting the diamond crystals, the rest of the contents of the capsule were filled with epoxy and polished. The structural and textural features of the samples were studied by scanning electron (Tescan MIRA 3 LMU, Brno, Czech Republic) and optical (Carl Zeiss Axio Imager Z2m, Jena, Germany) microscopy. The phase compositions of the samples were analyzed on a Tescan MIRA 3 LMU scanning electron microscope coupled with an INCA EDS 450 microanalysis system with an EDS X-Max-80 Silicon Drift Oxford Instruments detector. The accelerating voltage was 20 kV; the beam current was 1 nA; and the spot diameter was 2–5 μm for solid phases and 100 μm for quenched melts. The EDS spectra were optimized for quantitation using the standard XPP procedure built into the INCA Energy 450 software. The measurement error was 2 rel.%. The following standards were used: albite for Na; orthoclase for K; diopside for Mg and Ca; pyrope (O-145) for Si, Al and Fe; Cr-garnet (Ud-92); Mn-garnet (Mn-IGEM); spinel for Ni; and ilmenite for Ti. The mass ratios of the phases in the experiments were estimated using the least squares mass balance method for a limited number of system components: SiO_2, TiO_2, Al_2O_3, MgO, and CaO. The calculations were performed with allowance for the initial compositions of the mixtures and the resulting mineral phases,

without taking into account the buffer association, and gave the sum of squared residuals ≤1. The results of the analyses are presented in Tables 2 and 3.

Table 2. Experimental conditions and weight fractions of the synthesized phases.

Run No.	T (°C)	Duration (h)	fO_2	Capsule	Outer Container	Ol	Grt	Cpx	Opx	Mst	Prv	Liq
Ud-H_2O system												
704_8_1	1400	5	RRO	Pt+Re	Fe_2O_3	0.26	0.13	0.05	-	-	-	0.56
1176_5_1	1200	40	CW-CCO	Pt+Re	no	0.39	0.08	0.03	-	-	0.01	0.49
1666_3_3	1200	10	RRO	Pt+Re	Fe_2O_3	0.4	0.08	0.03	-	-	0.01	0.47
2223_2_1	1200	10	IRM	Au	no	0.34	-	0.16	-	-	-	0.5
Ud-OA system												
704_8_2	1400	5	RRO	Pt+Re	Fe_2O_3	0.09	-	0.37	-	0.26	-	0.28
1753_1	1200	40	CW-CCO	Pt+Re	no	n.d	n.d	n.d	n.d	n.d	n.d	n.d
1294_7_5	1200	10	RRO	Pt+Re	Fe_2O_3	0.04	0.01	0.36	0.03	0.35	0.01	0.2
2223_2_3	1200	10	IRM	Au	no	-	0.01	-	0.43	-	-	0.56
GS-H_2O system												
706_8_1	1400	5	RRO	Pt+Re	Fe_2O_3	-	-	-	-	-	-	1
1176_5_2	1200	40	CW-CCO	Pt+Re	no	-	-	-	-	-	-	1
1666_3_4	1200	10	RRO	Pt+Re	Fe_2O_3	-	-	-	-	-	-	1
2223_2_5	1200	10	IRM	Au	no	-	-	-	-	-	-	1
GS-OA system												
706_8_2	1400	5	RRO	Pt+Re	Fe_2O_3	-	-	-	-	-	-	1
2178_2_5	1200	40	CW-CCO	Pt+Re	no	-	-	-	-	-	-	1
1294_7_6	1200	10	RRO	Pt+Re	Fe_2O_3	-	-	-	-	-	-	1
2223_2_7	1200	10	IRM	Au	no	-	-	-	-	-	-	1

Pt+Re—Pt capsules lined with Re foil; -the phase is absent; n.d.—not determined; Ol—olivine; Opx—orthopyroxene; Cpx—clinopyroxene; Grt—garnet; Mst—magnesite; Prv—perovskite; Liq—melt.

Table 3. Compositions of phases and melts in experiments on the dissolution of diamonds.

Run No.	T (°C) Duration (h)	fO_2	Phase	SiO_2	TiO_2	Al_2O_3	Cr_2O_3	FeO	MnO	NiO	MgO	CaO	Na_2O	K_2O	Total
Ud-H_2O system															
704_8_1	1400 5	RRO	Ol	41.1	-	-	-	7.37	-	0.3	51.1	-	-	-	99.87
			Grt	42.3	0.9	19.68	2.57	4.61	-	-	18.7	10.7	-	-	99.46
			Cpx	55.1	0.2	2.39	0.33	2.08	-	-	17.6	20.3	1.3	-	99.3
			Liq	11.2	1.4	1.9	-	6.13	-	-	15.5	18.2	4.4	1.9	60.63
1176_5_1	1200 40	CW-CCO	Ol	40.3	-	-	-	9.1	-	0.2	49.5	0.2	0.2	-	99.5
			Grt	40	2.8	17.3	1.13	7.34	0.3	-	12.7	17.3	0.3	-	99.17
			Cpx	54.1	0.3	1.8	0.22	2.52	-	-	16.1	22.9	1.3	-	99.24
			Prv	-	58.7	0.33	-	1.6	-	-	39.2	-	-	-	99.83
			Liq	8.9	1	4.43	0.35	3.99	-	-	8.2	19.7	5.8	3.2	55.57
1666_3_3	1200 10	RRO	Ol	40.5	-	-	-	9.4	-	0.3	49.3	-	-	-	99.5
			Grt	40.4	2.2	17.73	1.17	6.63	0.2	-	10.8	19.8	0.3	0.2	99.43
			Cpx	54.2	0.3	1.86	0.32	2.19	-	-	16.2	22.9	1.1	-	99.07
			Prv	-	57.9	0.31	-	2.2	-	-	39.4	-	-	-	99.81
			Liq	8.1	-	2.18	-	1.74	-	-	7	18.7	4.4	2.7	44.82
2223_2_1	1200 10	IRM	Ol	40.2	-	-	-	10.53	-	0.2	48.6	0.1	-	-	99.63
			Cpx	54.8	0.3	1.77	0.26	4.45	-	-	16.7	19.4	1.5	-	99.18
			Liq	6.4	1	1.58	-	8.86	-	-	9.8	12.9	2.3	2.1	44.94

Table 3. *Cont.*

Run No.	T (°C) Duration (h)	fO_2	Phase	SiO_2	TiO_2	Al_2O_3	Cr_2O_3	FeO	MnO	NiO	MgO	CaO	Na_2O	K_2O	Total
Ud-OA system															
704_8_2	1400 5	RRO	Ol	40.7	-	-	-	9.83	-	0.3	48.9	0.1	-	-	99.83
			Cpx	56	0.5	2.33	0.25	3.9	-	-	20.7	14.5	1.6	-	99.78
			Mst	-	-	-	-	5.05	-	-	37.2	3.2	-	-	45.45
			Liq	2.9	0.4	1.38	-	5.53	-	-	12.8	21.4	5.2	2.8	52.41
1294_7_5	1200 10	RRO	Ol	40.8	-	-	-	8.19	-	0.3	50.2	-	-	-	99.49
			Cpx	54.6	0.3	2.58	0.5	2.67	-	-	17.4	19.5	1.5	-	99.05
			Opx	56.1	-	3.02	0.38	4.9	-	-	34.1	0.5	-	-	99
			Grt	41.8	1.78	20.16	1.06	7.67	0	0	19.84	7.14	0	0	99.45
			Mst	-	-	-	-	4.37	-	-	37.6	1.7	-	-	43.67
			Prv	-	54.21	0	0.72	2	0	-	1.48	38.9	1.42	0.48	99.21
			Liq	9	0.2	1.05	-	3.72	-	-	9.7	18.9	10.1	3.5	56.17
2223_2_3	1200 10	IRM	Opx	56.1	-	0.79	-	9.82	-	-	31	1.2	0.3	-	99.21
			Grt	42.5	1.4	18.88	1.68	14.81	0.3	-	15.4	5.1	0.2	-	100.27
			Liq	5.5	1.6	1.62	-	12.81	-	-	6.7	9.3	2.9	1.6	42.03
GS-H_2O system															
706_8_1	1400 5	RRO	Liq	0.7	-	0.85	-	3.32	-	-	3.7	14.9	0.4	26.5	50.37
1176_5_2	1200 40	CW-CCO	Liq	0.6	-	0.77	-	2.85	-	-	4	14.3	0.3	19.4	42.22
1666_3_4	1200 10	RRO	Liq	0.7	-	0.95	-	3.03	-	-	4.5	16.4	-	29.2	54.78
2223_2_5	1200 10	IRM	Liq	2.1	2.2	0.5	-	14.14	-	-	2.7	12.1	-	24.1	57.84
GS-OA system															
706_8_2	1400 5	RRO	Liq	1.8	-	1.96	-	3.68	-	-	4.4	16.8	0.5	18.5	47.64
1294_7_6	1200 10	RRO	Liq	0.7	-	0.82	-	3.42	-	-	3.8	14.2	0.3	22.6	45.84
2223_2_7	1200 10	IRM	Liq	1.9	1.9	0.47	-	17.68	0.3	-	2.8	11	-	22.7	58.75

3. Results

3.1. Phase Composition of Systems

All the phases of the buffer residing directly in the capsule with a sample remained stable at experimental P–T parameters, which ensured buffering fO_2 in the sample. In particular, after the experiments, ReO_2 was present on the surface of rhenium and throughout the sample, being indicative of the adequate functioning of the RRO buffer.

After the quenching of the samples containing Ud-H_2O, Ud-OA, GS-H_2O, and GS-OA systems, they comprise a dendritic aggregate of quenched carbonate and silicate phases and, in some cases, solid phases that are stable with a melt (Figures 3 and 4). Dendritic aggregates formed after melt quenching have a characteristic appearance for carbonate-silicate systems at high P–T parameters [36,38]. There are no signs of the transition of fluids/melts of the studied systems from a two-phase state to a supercritical fluid state. This is consistent with the findings [39] that the second critical point for the lherzolite-CO_2-H_2O system occurs at $p > 8$ GPa. Complete melting occurs in the GS-H_2O and GS-OA systems at experimental temperatures of 1200 and 1400 °C (Figure 4c,d). The systems with kimberlite (Ud) contain both simple and more complex five-phase (Ol–Cpx–Grt–Prv–L, Ud–H2O system, run no. 1666_3_3) and seven-phase (Ol–Cpx–Opx–Grt–Mst–Prv–L, Ud-

AO system, run no. 1294_7_5) associations (Table 2, Figure 4a,b). Perovskite is a common accessory phase in kimberlite-bearing samples (Figure 4a,b).

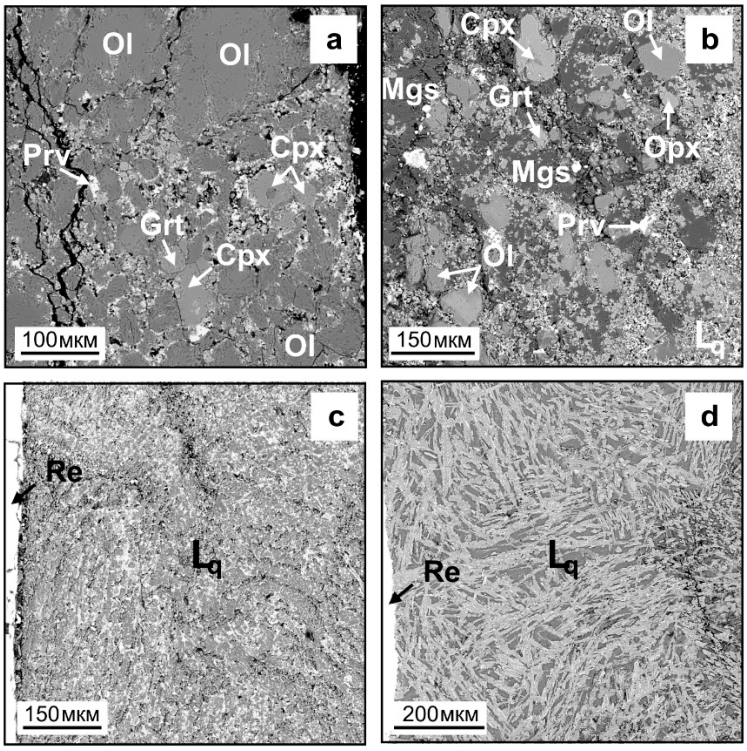

Figure 4. SEM images of the samples after the experiments. (**a**) Ud-H_2O system, Re-ReO_2 buffer, run no. 1666_3_3; (**b**) Ud-OA system, Re-ReO_2 buffer, run no. 1294_7_5; (**c**) quenched melt, GS-OA system, run no. 1294_7_6; and (**d**) quenched melt, GS-H_2O system, run no. 2223_2_6.

Table 2 provides the quantitative ratios of the melt and solid phases in the samples. There were no bubbles of a free fluid phase in the quenched samples, which indicates that fluid-undersaturated carbonate–silicate melts were present in all the experiments. The set of solid phases in equilibrium with a melt in the samples with Ud kimberlite depends on the volatile concentration, temperature, and oxygen fugacity. A melt multiphase saturated with respect to carbonated lherzolite was produced in the Ud-OA system at 1200 °C and fO_2 controlled by the RRO buffer. In this case, the addition of molecular CO_2 (as oxalic acid) to the system ensures the emergence of magnesite and orthopyroxene in the sample at 1200 °C. As the temperature in this system increases to 1400 °C, orthopyroxene disappears, and the melt becomes saturated with respect to carbonated wehrlite. It is noteworthy that an increase in fO_2 up to the IRM buffer values results in the complete carbonation of olivine and the disappearance of clinopyroxene in the Ud-OA system at 1200 °C. This probably occurs due to the fact that the CO_2/H_2O ratio in the system increases as fO_2 rises. The phase composition of the Ud-H_2O system after the experiments generally agrees with the data of our earlier studies focusing on the melting of kimberlite from the Udachnaya pipe with additions of H_2O [31]. In particular, most melts produced in the Ud-H_2O system at 1200 °C and fO_2 in the range between IRM and CW–CCO buffers were saturated with respect to garnet-bearing wehrlite. A similar picture was observed at 1400 °C and fO_2 of the RRO buffer. Only in the sample produced at 1200 °C under oxidized conditions of the IRM buffer, was there no garnet among the phases in equilibrium with the melt.

The melting degree of Ud-H_2O samples at 6.3 GPa and 1200–1400 °C varies in a relatively narrow range, from 48 to 56 wt% and, therefore, is independent of the redox conditions and composition of added volatiles. In contrast to this, the melting degree in two of the three samples in the Ud-OA system is noticeably lower (20–28 wt%). Only in the sample with the internal buffer IRM, did the melting degree increase to 56 wt%, and

the FeO concentration in the melt reached 12.8 wt% due to the interaction with buffer (enrichment of the system with iron). It is noteworthy that FeO content in the Ud-H_2O system containing the IRM buffer was 8.9 wt%. Thus, the melting degree of the samples produced in the presence of IRM cannot be directly compared to that of other samples. In one experiment at 1200 °C without buffer with fO_2 values between CW and CCO, the mass balance could not be calculated due to sample defragmentation.

The magnesian content of orthopyroxene and olivine in the samples obtained at 1200 °C ranges from 82–92 and 89–92, respectively. It is important to note that the presence of magnetite in the samples with IRM buffer leads to minimum Mg# values of olivine (89) and orthopyroxene (82). Olivine produced at 1400 °C has Mg# values of 90–92.5. Clinopyroxene in the samples is characterized by the Ca# lying in a range of 42–48 at 1200 °C and 31–43 at 1400 °C. Garnet from samples contains 1.1–2.6 wt% of Cr_2O_3, 5.1–19.8 wt% of CaO, and 4.6–14.8 wt% of FeO. Furthermore, the FeO concentration is maximal, and the CaO concentration is minimal in garnet from the sample with IRM buffer. In magnesite produced at 1200 °C and 1400 °C, FeO content is 4.3 and 5.0 wt%, and CaO content is 1.7 and 3.2 wt%, respectively. The melt composition ranges from largely carbonatitic to low SiO_2 carbonate–silicate (Figure 5). At 1200 °C and fO_2 of the IRM buffer, SiO_2 concentration in the melt varies from 6.4 wt% in the Ud-H_2O sample to 5.5 wt% in the Ud-OA sample (Figure 5). In Ud-H_2O samples, SiO_2 concentration slightly increases to 8 wt% at fO_2 of the RRO buffer and to 9 wt% at fO_2 of WC–CCO. Under the same redox conditions in GS-OA and GS- H_2O samples, the SiO_2 content is <2 wt%. At 1400 °C and fO_2 of the RRO buffer, SiO_2 concentration in a melt did not exceed 11 wt% in the Ud-H_2O system, and was below 3 wt% in the Ud-OA, GS-H_2O, and GS-OA systems.

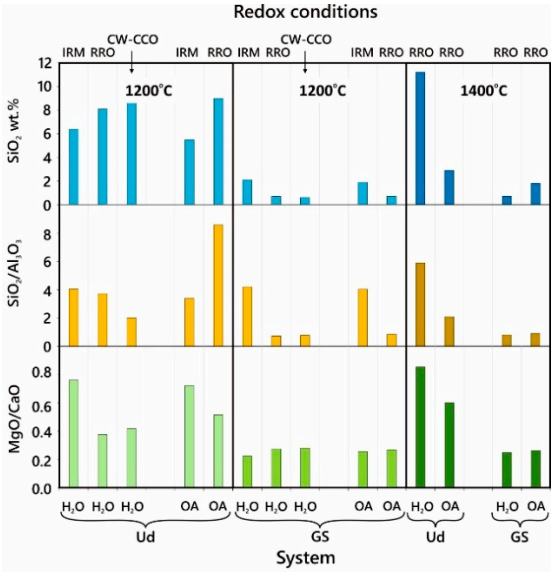

Figure 5. The compositions of the quenched carbonate–silicate melts obtained in experimental runs on the resorption of diamond crystals using kimberlite (Ud) and carbonatite (GS) with additions of H_2O or oxalic acid (OA) under various redox conditions.

The SiO_2/Al_2O_3 ratio reaches 6–8 in melts with the maximum SiO_2 content, and is below four in other cases. In this case, the MgO/CaO ratio does not exceed one in all the melts. The produced compositions are far from the "classical" kimberlite compositions on the diagram [40]. The compositions of all melts produced in the experiments are actually close to those of carbonatite metasomatic agents. Such melts from the Ud-OA and Ud-H_2O system were saturated with garnet lherzolite or wehrlite.

3.2. Diamond Resorption Morphology

In our experiments conducted under various T–fO_2 conditions, crystals lost from only a few percent to 98% of their initial weight. Most of the crystals have a weight loss ranging from 11% to 30% (Table 4), which allows one to compare the microreliefs produced at different fO_2 values.

Table 4. Experimental findings on diamond resorption.

Run No.	T (°C)	Duration (h)	fO_2	Diamond			
				Initial Weight (mg)	Final Weight (mg)	WL %	V
Ud-H_2O system							
704_8_1	1400	5	RRO	0.31 0.31	0.16 0.11	48 65	0.369 0.488
1176_5_1	1200	40	CW-CCO	0.33 0.33	0.29 0.28	12 15	0.011 0.014
1666_3_3	1200	10	RRO	0.30 0.30	0.26 0.25	13 16.5	0.048 0.060
2223_2_1	1200	10	IRM	0.36	0.21	42	0.170
Ud-OA system							
704_8_2	1400	5	RRO	0.29 0.29	0.23 0.24	21 17	0.148 0.123
1753_1	1200	40	CW-CCO	0.40	0.40	0	0
1294_7_5	1200	10	RRO	0.27 0.27	0.24 0.23	11 15	0.037 0.049
2223_2_3	1200	10	IRM	0.39	0.33	15	0.066
2223_2_4	1200	10	IRM	0.39	0.34	13	0.055
GS-H_2O system							
706_8_1	1400	5	RRO	0.34 0.34	0.05 0.01	85 97	0.672 0.764
1176_5_2	1200	40	CW-CCO	0.30 0.30	0.26 0.25	13 17	0.012 0.015
1666_3_4	1200	10	RRO	0.30 0.30	0.24 0.22	20 27	0.072 0.980
2223_2_5	1200	10	IRM	0.36	0.24	33	0.136
GS-OA system							
706_8_2	1400	5	RRO	0.25 0.25	0.13 0.01	48 96	0.308 0.615
2178_2_5	1200	40	CW-CCO	0.38	0.38	<2	<0.003
1294_7_6	1200	10	RRO	0.30 0.30	0.22 0.24	27 20	0.096 0.072
2223_2_7	1200	10	IRM	0,36	0,26	27	0.113
2223_2_8	1200	10	IRM	0.36	0.27	25	0.102

WL—weight loss of diamond; V—diamond resorption rate (mg/mm^{2}min^{-1}) $\times 10^3$.

There are negative trigons on the octahedron faces of all crystals, where they are preserved as relics. Trigons are triangular etch pits of which the contour is oriented negatively with respect to the contour of the octahedron faces. There are two types of trigons [41]. Some trigons have a flat bottom and are called flat-bottomed trigons (f.b. trigons). Trigons of the second type are pyramidal, lack a flat bottom, and are called pyramidal or point-

bottomed trigons (p.b. trigons). P.b. trigons are abundant on crystals with a small degree of dissolution, and their size (diameter) does not exceed 5 μm in most cases. Larger p.b. trigons, up to 40 μm in size, occur as single trigons on more significantly resorbed crystals. The profile of typical trigons is shown in Figure 6a–d.

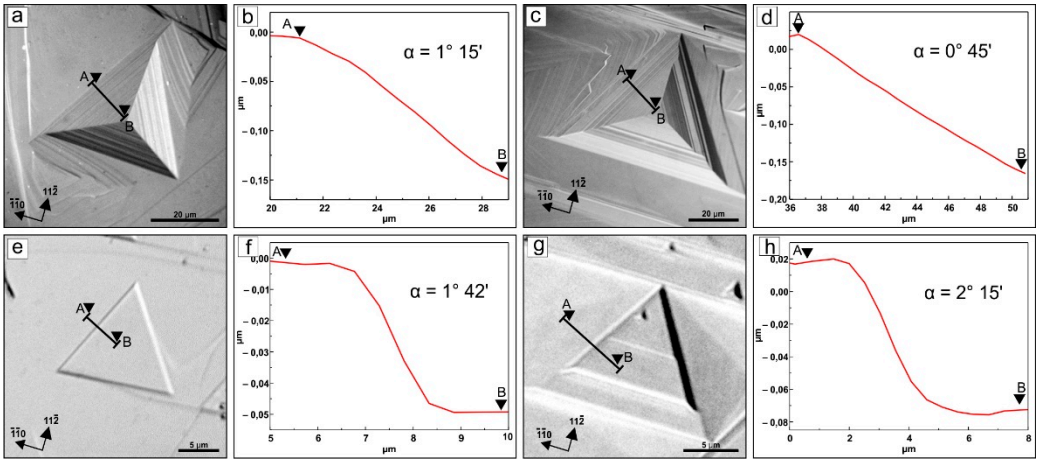

Figure 6. DIC images (**a**,**c**,**e**,**g**) and cross-sectional profiles (**b**,**d**,**f**,**h**) of typical trigons on the octahedral faces of diamond crystals after the experiments: (**a**–**d**) point-bottomed trigons; (**e**–**h**) flat-bottomed trigons.

According to TIC measurements, the angle α between the p.b. trigon walls and the octahedron face is 0.5–3.5° in the entire range of redox conditions used. The size of flat-bottomed trigons ranges from 5 to 100 μm. Small f.b. trigons are characterized by different degrees of vertex truncation, and their walls have the same inclination angles as those in p.b. trigons (Figure 6e–h). Larger f.b. trigons have steep stepped walls whose inclination angles vary considerably, from 10° to 60°. Large flat-bottomed pits are usually not deep. The larger f.b. trigons are, the smaller their amount on the crystal faces is. It should be noted that the amount and distribution of trigons on different faces of the same crystal are different. Some crystal faces are covered with numerous trigons, whereas others are almost free of trigons (Figure 7).

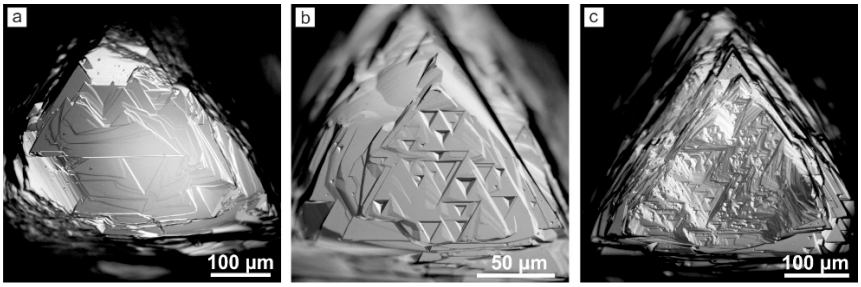

Figure 7. DIC images of {111} faces of one diamond crystal after resorption in the GS-H_2O system (run no. 1176_5_2): (**a**) the face without trigons; (**b**) the face with a small number of large trigons; (**c**) the face with many small trigons.

Simultaneously with trigon formation, dissolution layers are developed on the octahedron faces. The directions of layer ends slightly deviate from the <110> directions that correspond to the position of octahedron edges upon a small loss of the initial crystal weight (Figure 8d,h,j). The contour of the layers changes as the degree of resorption increases, and the layers acquire a shield-like or ditrigonal shape (Figures 8k,p and 9f,j). In the case of the polycentric arrangement of dissolution layers on the octahedron faces, serrated sculptures are often formed near the crystal vertices (Figures 8h,n and 9h). The octahedron edges are truncated by curved surfaces of a tetrahexahedroid. These surfaces often have a

rounded stepped relief composed of alternating coarsely stepped and relatively smooth rounded areas (Figures 8c,g and 9c,e). Sometimes, rounded stepped surfaces are covered with uniform striation formed by the dissolution layer ends (Figures 8m,o and 9i).

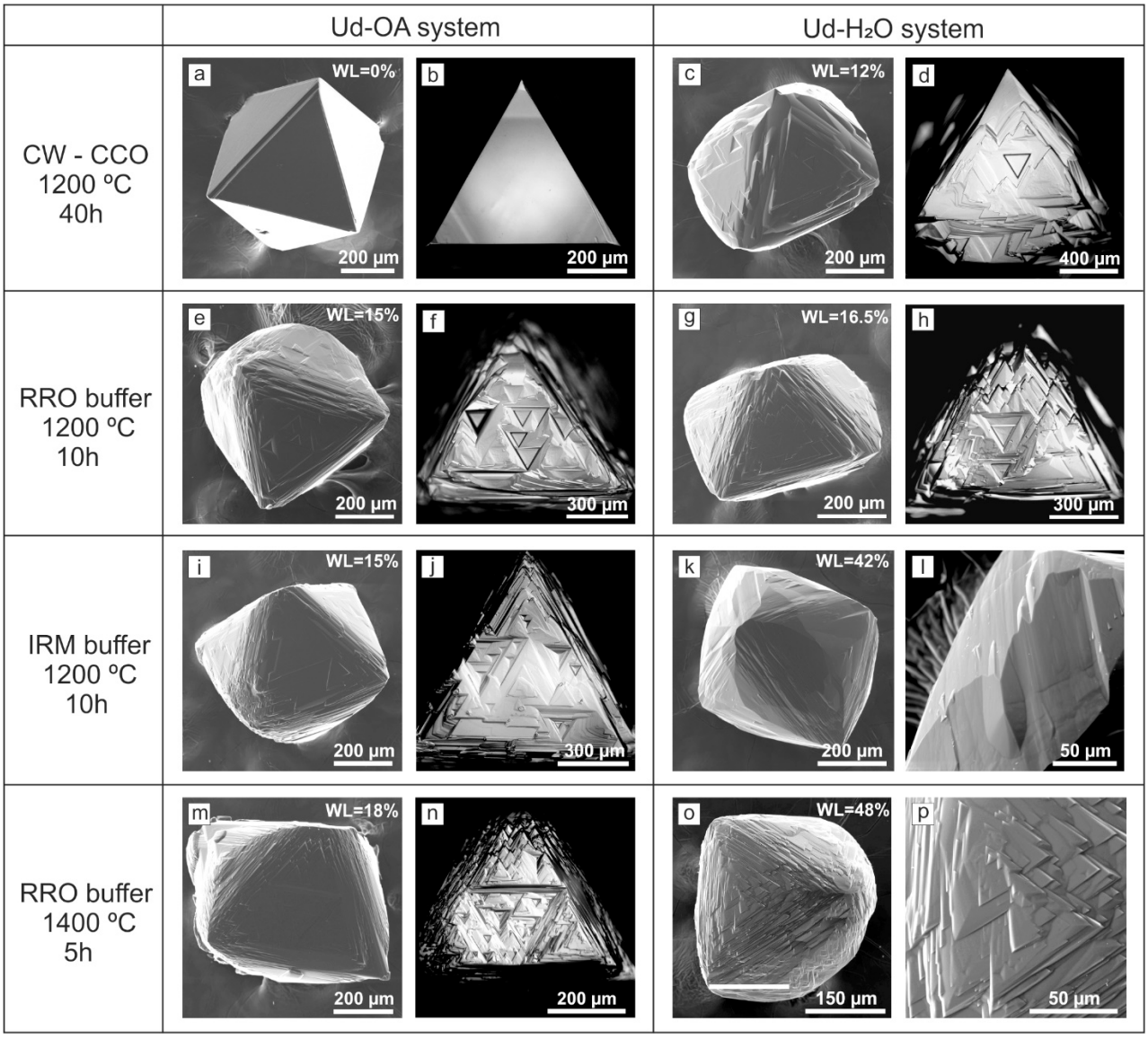

Figure 8. Micrographs of diamond crystals after partial resorption in the Ud-H_2O and Ud-OA systems. (**a**) Octahedral crystal without resorption patterns from experimental run no. 1753_1 and (**b**) its face in reflected light; (**c**) crystal from experimental run no. 1176_5_2 and (**d**) its (111) face in reflected light; (**e**) crystal from experimental run no. 1294_7_5 and (**f**) its (111) face in reflected light; (**g**) crystal from experimental run no. 1666_3_3 and (**h**) its (111) face in reflected light; (**i**) crystal from experimental run no. 2223_2_3 and (**j**) its (111) face in reflected light; (**k**) tetrahexahedroid from experimental run 2223_2_1 and (**l**) the fragment of its surface; (**m**) crystal from experimental run no. 704_8_2 and (**n**) its (111) face in reflected light; (**o**) tetrahexahedroid crystal from experimental run no. 704_8_1 and (**p**) a fragment of its surface. WL—weight loss of diamond.

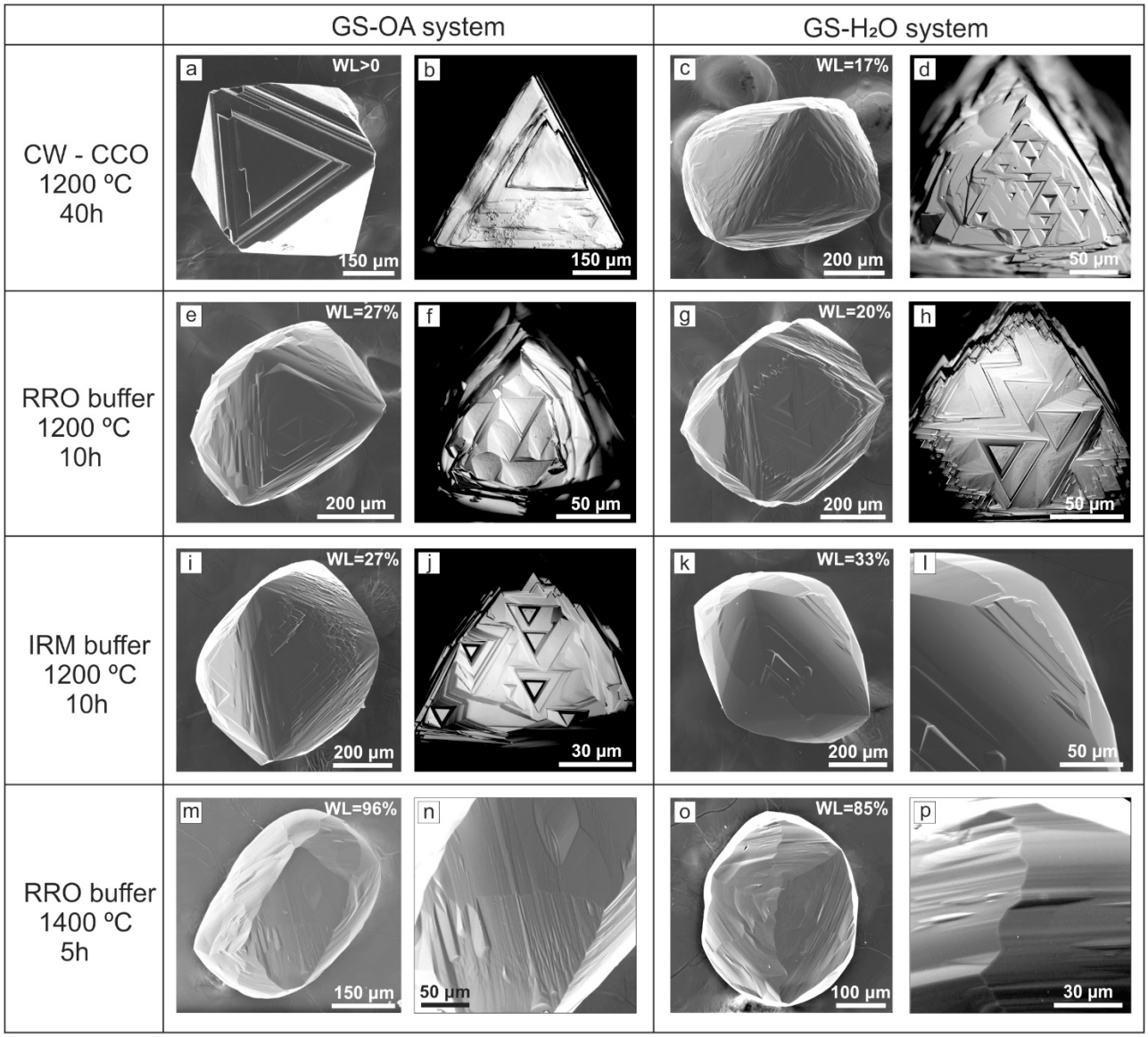

Figure 9. Micrographs of diamond crystals resorbed to varying degrees in GS-H_2O and GS-OA systems. (**a**) Slightly resorbed octahedron from run no. 2178_2_5 and (**b**) its (111) face in reflector light; (**c**) crystal from run no. 1176_5_2 and (**d**) its (111) face in reflected light; (**e**) crystal from run no. 1294_7_6 and (**f**) its (111) face in reflected light; (**g**) crystal from run no. 1666_3_4 and (**h**) its (111) face in reflected light; (**i**) crystal from run no. 2223_2_7 and (**j**) its (111) face in reflected light; (**k**) tetrahexahedroid with mirror-smooth surface from run no. 2223_2_5 and (**l**) fragment its surface; (**m**) tetrahexahedroid from run no. 706_8_2 and (**n**) fragment its surface; (**o**) crystal from run 706_8_1 and (**p**) fragment of its tetrahexahedroid surface. WL—weight loss of diamond.

Near the <100> vertices, parallel striation is transformed into hackly striation. Often, there are dissolution hillocks with varying degrees of elongation (Figures 8c,l and 9n,o). The newly formed rounded surfaces are sometimes mirror-smooth (Figure 9k,l). We found no fundamental differences in the relief of rounded surfaces of diamonds resorbed in the investigated T–fO_2 interval. The octahedron faces completely disappear when the loss of the initial crystal weight is more than 30%. (Figures 8k and 9k). Crystals acquire the tetrahexahedroid shape with distinct vertices and apparently resemble the so-called natural diamond octahedroid. In the case of significant dissolution, the shape of crystals becomes spherical, with more uniform roundness of tetrahexahedroid surfaces

(Figure 9m,o). They clearly display edges and vertices, which enables assigning this form to a spherical tetrahexahedroid or the so-called Brazilian or Ural type diamonds [42].

3.3. Dependence of the Resorption Rate on fO_2

The diamond resorption rates in the entire range of used fO_2 were studied at a temperature of 1200 °C. The obtained values are given in Table 4 and summarized as a plot in Figure 10. The diamond resorption rates are the lowest under the least oxidizing conditions controlled by the range of fO_2 from the water maximum (WC) to the CCO equilibrium. In water-bearing systems (Ud-H_2O and GS-H_2O), the resorption rates lie within 0.011–0.015 mg/mm^2 min^{-1} × 10^3. After the experiments in the systems with the addition of oxalic acid, fine-crystalline graphite was present on the surface of diamond crystals, which covered some of the diamond crystal faces. After these experiments, no loss of crystal weight was found. Diamond resorption in the GS-OA system was detected through insignificant changes in the microrelief, whereas no changes in the relief of diamond faces were found in the Ud-OA system.

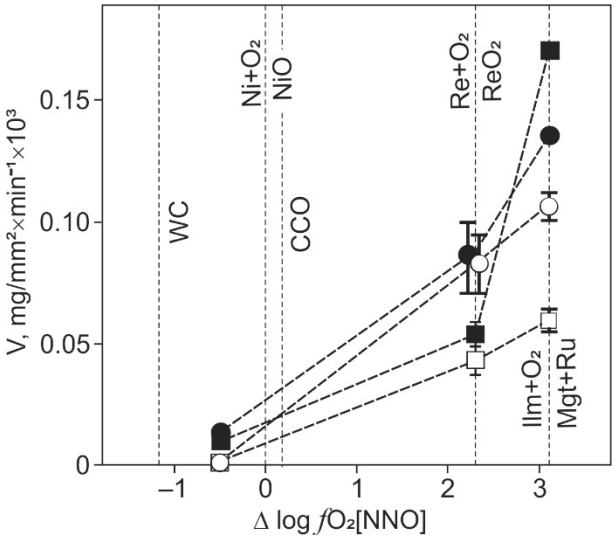

Figure 10. The resorption rate of octahedral crystals of natural diamond in experimental runs at 1200 °C and 6.3 GPa depending on fO_2. Solid squares—Ud-H_2O system; open squares—the Ud-OA system; solid circles—the GS-H_2O system; and open circles—the GS-OA system. Vertical bars show the range of dissolution rates for two diamond crystals.

A rise in fO_2 to the RRO buffer values significantly increased the resorption rate in all the systems. Under these redox conditions, melts in the GS-H_2O and GS-OA systems were most active to diamond; the resorption rates in them increased to 0.072–0.096 mg/mm^2 min^{-1} × 10^3, and the mass of crystals decreased by 20–27%. Melts in the Ud-H_2O and Ud-OA systems were less aggressive to diamond. The resorption rates in these systems were 0.037–0.060 mg/mm^2 min^{-1} × 10^3, and the mass of crystals decreased by 11–16%.

A rise in fO_2 to the IRM buffer level further increased the rate of diamond resorption. The highest rates were observed in melts in the water-bearing systems Ud-H_2O and GS-H_2O. In this case, the resorption rate reached the maximum value of 0.170 mg/mm^2 min^{-1} × 10^3 in the Ud-H_2O system. The minimum resorption rates of 0.055–0.066 mg/mm^2 min^{-1} × 10^3 were found in melts of the Ud-OA system.

3.4. Temperature Dependence of the Resorption Rate

The temperature dependence of the resorption rate was studied at fO_2 of the RRO buffer (Table 5; Figure 11a). A temperature rise from 1200 to 1400 °C increases the resorption rate. The maximum increase in the resorption rate was found in the GS-H_2O system. The rate increased tenfold and was 0.672–0.764 mg/mm^2 min^{-1} × 10^3, and diamond

crystals lost from 87% to 98% of their initial weight within 5 h. In this system at 1200 °C, diamond crystals of the same weight lost only 20% of their initial weight within 10 h. The minimum increase in the resorption rate was found in melts of the Ud-OA system. Elevation of temperature by 200 °C in the system increased the rate of diamond resorption approximately threefold, to 0.123–0.148 mg/mm^2 min^{-1} × 10^3. The loss of the initial crystal weight was 18–21%. The rate of diamond resorption in the GS-OA and Ud-H_2O systems increases four- to eightfold, as the temperature is elevated from 1200 °C to 1400 °C.

Table 5. Activation energy of diamond resorption at fO_2 = RRO buffer.

Pressure, GPa	Activation Energy of Diamond Resorption, kJ/mol			
	Ud-H_2O System	Ud-OA System	GS-H2O System	GS-OA System
3.0 [1]	125	195	240	260
6.3	215	120	240	170

[1] Activation energy values from [23].

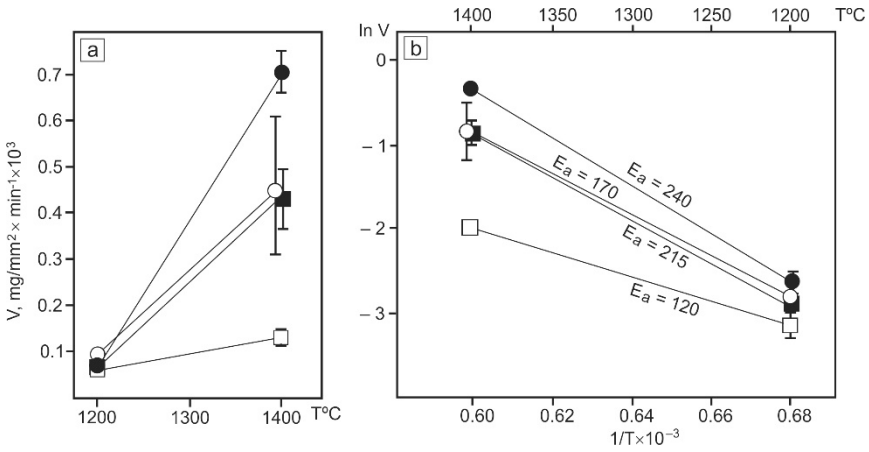

Figure 11. Temperature dependence of diamond resorption rates (**a**) and the Arrhenius plot (**b**) of the resorption rates under redox conditions controlled by RRO buffer: solid squares—the Ud-H_2O system; open squares—the Ud-OA system; solid circles—the GS-H_2O system; and open circles—the GS-OA system.

As mentioned in the Material and Methods section, we placed two diamond crystals of the same initial weight and appearance into all platinum capsules. After the experiments, there was a difference in the loss of the initial weight by crystals, even when they were in close proximity to each other. Usually, these differences were small. In some cases, however, an initial weight loss and, accordingly, changes in the resorption rate were very significant. The widest scatter in resorption rates of diamond crystals present in the same capsule was observed at 1400 °C. Moreover, the most significant differences in resorption ability were found in diamonds from experimental run no. 706_8_2 (the GS-OA system). Losses of the initial weight of crystals differed twofold, and were 49% and 98%. The diamond crystals were located in one part of the capsule and, accordingly, under the same resorption conditions. Therefore, the revealed differences in the resorption rates are most likely to be associated with the individual characteristics of crystals, such as the defect-impurity composition, the dislocation structure, and the presence of other defects in the diamond crystal lattice. In connection with the established spread in the rates of diamond resorption, our estimate of the activation energies of this process is only preliminary, and requires further refinement.

4. Discussion

4.1. Diamond Resorption Morphology

It has been experimentally shown that rounded diamond tetrahexahedroids, similar to natural rounded diamonds, can be formed at pressures from 1 GPa to 6.3 GPa and temperatures from 1200 °C to 1500 °C [3,11]. However, there are some specific features in the diamond morphology and resorption process, which occurred at different pressures and in different media. At pressures of 1–2 GPa, free water-bearing fluid is the main factor controlling the formation of diamond tetrahexahedroids [43]. At higher pressures (3–6 GPa), spherical tetrahexahedroids can be formed both in an aqueous fluid [12,44] and in water-bearing carbonate–silicate melts [15,23]. Tetrahexahedroids can have a glossy surface or display other relief elements, depending on the actual structure of diamond crystals and dissolution conditions. An increase in pressure from 1 to 3 GPa accelerates the transformation of an octahedral crystal into a tetrahexahedroid [44]. However, a comparison of the results of this study to earlier findings [15,23] indicates that a further increase in pressure does not accelerate this transformation. The initial octahedron faces disappear in diamond dissolution forms as an octahedral crystal loses 25–30% of its initial weight, both at a pressure of 3 GPa [23] and at a pressure of 5.7–6.3 GPa [15]. Only upon diamond resorption in an aqueous fluid at 5 GPa, do the octahedron faces disappear at a loss of the initial diamond weight of about 50% [12], like in the experiments at 1 GPa. Hence, it can be inferred that the rate of transformation of octahedral diamond into a spherical tetrahexahedroid weakly depends on pressure, and is largely controlled by the composition of the medium that it interacts with. The transformation rate of a starting flat-faced crystal increases as the resorption medium changes from a fluid to a volatile-rich carbonate–silicate melt. In this case, the sculpture of the octahedron faces changes. When a diamond is resorbed in a fluid at 1–5 GPa, layer-by-layer resorption is weak. There are distinct edges between the relic octahedral faces and the newly formed surfaces of tetrahexahedroids. In other words, there is no smooth transition of octahedral faces to the rounded tetrahexahedral shape. Therefore, resorption occurs mainly due to the truncation of the octahedron edges by the newly formed tetrahexahedroid surfaces. These distinctive features were noted earlier in [3]. During resorption in H_2O and CO_2-bearing carbonate–silicate melts, numerous dissolution layers are present on octahedral surfaces. They are formed due to layer-by-layer dissolution on the octahedral faces. An echelon of steps is formed near the edges of the octahedron, leading to a smooth transition of the octahedral faces to the surfaces of the tetrahexahedroid. As a result, the octahedral faces disappear more quickly when diamond is dissolved in H_2O- and CO_2-bearing carbonate–silicate melts than in a fluid.

The presence or absence of trigons on the octahedron faces, as well as their number and size, is determined mainly by the dislocation structure of diamond crystals [45–47]. As shown in our work, the size and number of trigons can vary significantly, even on different faces of the same crystal. External conditions such as the medium composition, the redox conditions, and temperature can mainly affect the shape of etch pits (trigons).

4.2. Diamond Resorption Rate

We have shown that the diamond resorption rate increases as oxygen fugacity rises. However, not only fO_2 but the melt composition was changed in the investigated systems (Figure 5). In melts of the Ud-H_2O and Ud-OA systems, an increase in fO_2 is accompanied by a reduction in SiO_2 concentration and an increase in FeO content. In particular, in a melt from the Ud-H_2O system at 1200 °C, the SiO_2 content decreases from 8.9 wt% to 6.4 wt%, and the FeO content increases from 4.0 wt% to 8.9 wt%, as fO_2 rises from CW—CCO to IRM buffer. In essentially carbonatite melts, FeO content increases even more significantly. For example, in a melt from the GS-H_2O system, as fO_2 is raised from CW–CCO to IRM buffer, the FeO content increases from 2.8 wt% to 14.1 wt%, and the SiO_2 content slightly increases from 0.6 wt% to 2.1 wt%. Because Fe ions act as catalysts and Si ions inhibit diamond oxidation during the catalytic oxidation of diamonds at p = 1 atm [48,49], it can

be inferred that concentration variations in the FeO and SiO_2 melt are an additional factor affecting the diamond resorption rate.

Our results and the previously reported data on the resorption rates under fixed redox conditions [18,23,43,44] make it possible to analyze the pressure dependence of the diamond resorption rate. Figure 12 shows diamond resorption rates at pressures ranging from 1 GPa to 6.3 GPa. Given the dependence of resorption rates on redox conditions, a comparison was performed at an fO_2 value of the NNO buffer, which is typical of deep-seated carbonate-silicate melts [26]. This choice is also related to the fact that reliable rates of diamond resorption in a fluid at pressures from 1 GPa to 3 GPa were obtained only for fO_2 = NNO –0.1 ÷ –0.6 [43,44]. The resorption rates in CO_2- and H_2O-bearing melts at 3 GPa and 6.3 GPa for fO_2 = NNO were estimated based on the dependences reported in [23]. Figure 12 shows that the diamond resorption rate decreases as pressure increases from 1 GPa to 6.3 GPa, even with a very significant spread in diamond resorption rates at a pressure of 1 GPa. However, the resorption rates at 1 GPa and 2 GPa [43,44] are obtained at temperatures of 1250 °C and 1350 °C, respectively, and are characteristic of diamond resorption in an aqueous fluid. At these pressures, there is no diamond resorption in melts lacking volatiles [43]. At higher pressures of 3–6.3 GPa, diamond resorption proceeds efficiently, both in free aqueous fluid [12] and in volatile-undersaturated carbonate–silicate melts. It is noteworthy that diamond resorption was observed even in a silicate melt with 0.4 wt% H_2O [13].

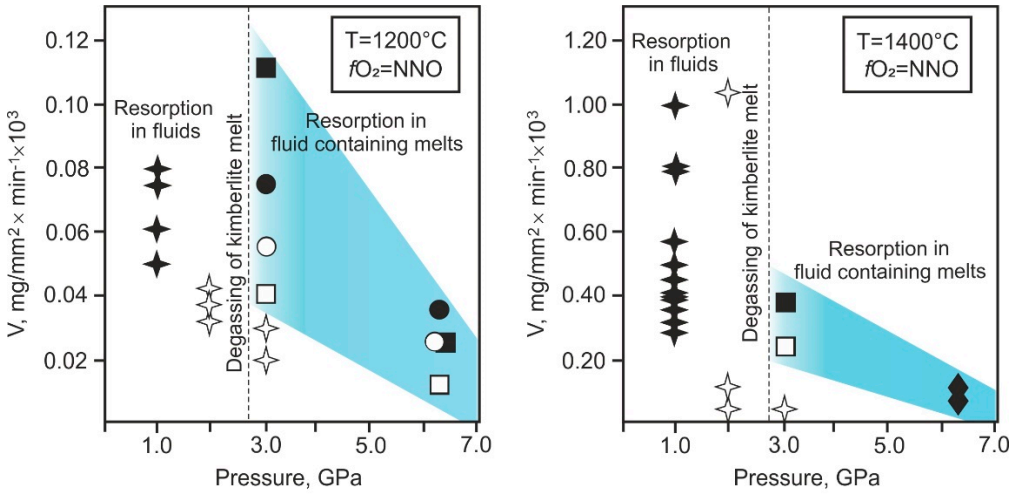

Figure 12. The pressure dependence of the diamond resorption rate at 1200 °C and 1400 °C and oxygen fugacity corresponding to the NNO buffer. The results of this study and according to the data reported in [23]: solid squares—the Ud-H_2O system; open squares—the Ud-OA system; solid circles—the GS-H_2O system; and open circles—the GS-OA system. Solid stars—resorption of diamond in H_2O and CO_2 fluids according to Fedortchouk et al. [43]; open stars—resorption of diamond in H_2O fluids according to Zang et al. [44]; solid rhombi—resorption of diamond in the Ud-H_2O system according to Sokol et al. [18]. Degassing pressure of ascending kimberlitic magma at pressures of 2–3 GPa is based on the data reported in [50]. The values of diamond resorption rates at 3 GPa according to Khokhryakov et al. [23].

To a first approximation, the oxidation of diamond with water vapor at 1 atm may be regarded as a reaction yielding carbon dioxide and hydrogen [48]. If we assume that diamond oxidation occurs at higher pressures via a similar mechanism, then a decrease in the rate of diamond resorption with increasing pressure in fluid systems may be explained using the principles of chemical kinetics. As long as the free fluid phase is stable, increasing pressure is known to shift the equilibrium of the reactions involving gaseous substances towards a smaller total number of gas moles. In the diamond oxidation reaction, two moles of water give three moles of gaseous reaction products. In this case, an increase in pressure in the reaction system will shift the equilibrium to the right side of the equation, and then

the reaction rate should decrease. However, these considerations are not applicable to diamond resorption in CO_2- and H_2O-bearing silicate–carbonate melts because there is no free fluid phase in the samples before and after dissolution. In this case, a decrease in the resorption rate with increasing pressure may be associated with changes in the dissolution form of water and CO_2 in a melt. The addition of molecular CO_2 (as oxalic acid) into the system ensured the emergence of magnesite in it and the formation of a carbonate–silicate melt depleted in SiO_2. Water dissolves in silicate melts mainly as molecular H_2O at low pressure and hydroxyl species at high pressure [51–53]. Silicate melts can dissolve CO_2 as carbonate and molecular CO_2 species [52,54]. Molecular CO_2 in a carbonate-silicate melt can be converted to carbonate particles, as the concentration of SiO_2 in it increases according to a homogeneous reaction [55]:

$$CO_2 + 2Q^n(M^{m+}) \leftrightarrow {CO_3}^{2-}(M^{m+}) + 2Q^{n+1} \quad (1)$$

where Q^n is a silica tetrahedron linked by bridging O atoms to n adjacent tetrahedra (zero n corresponds to an isolated SiO_4 tetrahedron); M^{m+} indicates alkali or alkali Earth cations associated with non-bridging oxygen in Q^n species and with oxygen in the ${CO_3}^{2-}$ complex. The decrease in the resorption rate in our experiments after oxalic acid had been added (the Ud-OA and GS-OA systems) as compared to the experiments with water added (the Ud-H_2O and GS-H_2O systems) is apparently associated with a lower concentration of water in these melts, which was about 2 wt% in the Ud-OA and GS-OA systems.

The resorption rates obtained at 1200 °C and 1400 °C under redox conditions of RRO buffer allow us to estimate the effective energy of diamond resorption in the studied systems. As we have already noted, the estimation of the activation energies of the resorption process was only preliminary due to the scatter of diamond resorption rates determined by us in this work and in previous studies at a pressure of 1.0–3.0 GPa [43,44]. Figure 11b shows the Arrhenius plot for the results. The graphically determined activation energies are presented in Table 4. The activation energy of diamond resorption in water-bearing melts is approximately 215–240 kJ/mol, which is significantly higher than the activation energy in H_2O- and CO_2-bearing melts (120–170 kJ/mol). It is interesting to compare the new findings with our earlier data on the activation energy of diamond resorption under similar conditions in the same systems, but at a pressure of 3.0 GPa [23]. The activation energy of the process remained unchanged only for diamond resorption in a water-bearing carbonatite melt (the GS-H_2O system). The constancy of the activation energy in this system may be indicative of the invariability of the diamond resorption mechanism at 3.0 and 6.3 GPa. A twofold decrease in the resorption rate with rising pressure is apparently associated with the kinetics of the diamond oxidation reaction. In the other studied systems, both a decrease (the Ud-OA and GS-OA systems) and an increase (the Ud-H_2O system) in the activation energy were observed. In this case, an increase in pressure is accompanied by a decrease in the resorption rates in all systems. The highest activation energy (425 kJ/mol) and higher rates were found for diamond resorption in an aqueous fluid at 1 GPa [43]. Large variations in the effective activation energies of diamond resorption are apparently associated with the features of diamond resorption mechanisms, depending on the bulk composition of melts, P–T–fO_2 conditions, and individual characteristics of crystals. Discussion of these issues is a rather non-trivial task and lies beyond the scope of this article.

4.3. Natural Resorption of Diamond

Our findings on the rates and features of diamond resorption in carbonate and carbonate–silicate melts in a wide range of pressures provide genetic information about the processes and mechanisms of natural diamond dissolution. Diamond resorption with the formation of tetrahexahedroids in nature might occur in the entire time interval, from the moment of their emergence in the mantle to their removal by magma to the surface. Diamond crystallization under mantle conditions at a pressure of 6 GPa and temperature of 1400 °C was experimentally implemented in various model systems (e.g., reviews [11,56]). Diamond growth can periodically give way to the partial resorption of crystals. The latter

may lead to significant morphological changes, including the formation of rounded diamonds. Our findings indicate that resorption might occur over a long period of time at relatively low rates. It might be caused by mantle metasomatism with the involvement of oxidizing agents with fO_2 above CCO. The possibility of this process is confirmed by the findings of oxidized mantle metasomatic rocks [57,58]. In upper mantle settings, carbonatite melts or fluids may be such oxidized metasomatic agents [59,60].

The well-known large type IIa and IIb gem diamonds from South African kimberlite deposits and kimberlites in Lesotho are the most vivid example of significant mantle resorption of diamond [61–63]. Weighing several hundred carats, these diamonds have a rounded dodecahedral habit (tetrahexahedroids). Consider, for example, the famous 550-carat blue diamond called the Letšeng Star. According to the experimental data, flat-faced diamond crystals are transformed into such spherical tetrahexahedroids upon the resorption of at least 45% of their initial weight [15,64]. Therefore, the Letšeng Star diamond was formed from an initial crystal with a weight of about 1380 carats. According to the experimentally determined resorption rates [23], an octahedral diamond crystal with an initial weight of 1380 carats in a water-bearing carbonate–silicate melt at 3 GPa, 1400 °C and fO_2 = NNO ± 1.5 log units would lose 45% of its original weight and would be transformed into a spherical tetrahexahedroid weighing about 550 carats over a period of more than 6 months. At a pressure of 6.3 GPa and other parameters being the same, the time of diamond resorption to be transformed into a spherical tetrahexahedroid should be at least two years. If two years is an insignificant period for mantle residence, 6 months, apparently, is an unreasonably long time for the kimberlite magma ascent.

At the initial stage of the formation of kimberlite melts, when their composition was close to that of volatile-rich carbonatites [65,66], both the crystallization and resorption of diamond may occur depending on the redox conditions and carbon content. COH-fluids and alkali-enriched essentially carbonate melts depleted in SiO_2 were experimentally shown to be capable of providing diamond growth at temperatures of 1400–1500 °C and pressures of 6.3–7.5 GPa [67–69]. At similar parameters and fO_2 above the CCO buffer in a melt, diamond might undergo significant resorption. Our studies have demonstrated that water-bearing carbonatite melts are the most active media with respect to diamonds under these conditions. Diamond resorption continued at an ever-increasing rate as volatile-rich kimberlite magma rose to depths of about 100 km. At pressures less than 3 GPa, after boiling up of kimberlite magma, a free fluid should have appeared, which apparently is the main agent of diamond resorption. As experimentally shown by Fedorchouk et al. [43], volatile-undersaturated carbonate–silicate melts cannot cause diamond resorption at a pressure of 1 GPa. However, it is difficult to expect significant changes in the morphology of transported diamonds after the boiling up of kimberlite magma, due to the high rate of its rise, even at the maximum resorption rates detected at a pressure of 1 GPa.

5. Conclusions

Therefore, we have found that rounded diamond tetrahexahedroids, similar to natural rounded diamonds, can be formed at pressures from 1 GPa to 6.3 GPa and temperatures from 1200 °C to 1500 °C. The rate of transformation of an initial octahedral crystal into a spherical tetrahexahedroid increases as the resorbing medium changes from a fluid to a H_2O- and CO_2-bearing carbonate–silicate melt. The rate of diamond resorption was experimentally shown to steadily decrease as pressure increased from 1 GPa to 6.3 GPa. Based on the experimental findings, we suggest that the resorption of the natural diamond may occur within the entire time interval, from the moment of diamond crystal formation in the mantle until the moment of their removal to the surface. During mantle metasomatism, as fO_2 and the agent composition changed, the stage of diamond crystallization might periodically have been replaced by the stage of partial or significant resorption. The resorption process that occurred for a long time, even at relatively low rates, might lead to the formation of rounded diamonds. Mantle metasomatism by the oxidized agent and the

initial stages of kimberlite magma ascent might contribute most significantly to diamond resorption and the formation of their tetrahexahedral shape.

Author Contributions: Conceptualization, A.F.K.; methodology, A.F.K. and A.G.S.; investigation, A.N.K. and D.V.N.; visualization, A.F.K., A.N.K. and A.G.S.; formal analysis, A.N.K. and D.V.N.; writing—original draft preparation, A.N.K., A.G.S. and D.V.N.; writing—review and editing, A.F.K. and A.G.S. All authors have read and agreed to the published version of the manuscript.

Funding: This research was funded by the Russian Science Foundation (grant number 19-77-10023).

Institutional Review Board Statement: Not applicable.

Informed Consent Statement: Not applicable.

Data Availability Statement: Not applicable.

Conflicts of Interest: The authors declare no conflict of interest. The funders had no role in the design of the study; in the collection, analyses, or interpretation of data; in the writing of the manuscript, or in the decision to publish the results.

References

1. Fedortchouk, Y.; Zang, Z. Diamond resorption: Link to metasomatic events in the mantle or record of record of magmatic fluid in kimberlitic magma? *Can. Mineral.* **2011**, *49*, 707–719. [CrossRef]
2. Fedortchouk, Y.; Liebske, C.; McCammon, C. Diamond destruction and growth during mantle metasomatism: An experimental study of diamond resorption features. *Earth Planet. Sci. Lett.* **2019**, *506*, 493–506. [CrossRef]
3. Fedortchouk, Y. A new approach to understanding diamond surface features based on a review of experimental and natural diamond studies. *Earth-Sci. Rev.* **2019**, *193*, 45–65. [CrossRef]
4. Smit, K.V.; Shirey, S.B. Diamond from the deep. *Gems. Gemol.* **2020**, *56*, 148–155.
5. Fedortchouk, Y.; Chinn, I.L.; Perritt, S.H.; Zhang, Z.; Stern, R.A.; Li, Z. Diamond-destructive mantle metasomatism: Evidence from the internal and external textures of diamonds and their nitrogen defects. *Lithos* **2022**, *414–415*, 106616. [CrossRef]
6. Robinson, D.N. Surface Textures and Other Features of Diamonds. Ph.D. Thesis, The University of Cape Town, Cape Town, South Africa, 1979; 221p.
7. Bulanova, G.P. Formation of diamond. *J. Geochem. Explor.* **1995**, *53*, 1–23. [CrossRef]
8. Chinn, I.L. A study of unusual diamonds from the George Creek K1 Kimberlite Dyke, Colorado. Ph.D. Thesis, University of Cape Town, Cape Town, South Africa, 1995; p. 94.
9. Haggerty, S.E. Diamond genesis in a multiply constrained model. *Nature* **1986**, *320*, 34–38. [CrossRef]
10. Gurney, J.J.; Hildebrand, P.R.; Carlson, J.A.; Fedortchouk, Y.; Dyck, D.R. The morphological characteristics of diamond from the Ekati property, Northwest Territories, Canada. *Lithos* **2004**, *77*, 21–38. [CrossRef]
11. Palyanov, Y.N.; Khokhryakov, A.F.; Kupriyanov, I.N. Crystallomorphological and crystallochemical indicators of diamond formation conditions. *Crystallogr. Rep.* **2021**, *66*, 142–155. [CrossRef]
12. Kanda, H.; Yamaoka, S.; Setaka, N.; Komatsu, H. Etching of diamond octahedrons by high pressure water. *J. Cryst. Growth* **1977**, *38*, 1–7. [CrossRef]
13. Khokhryakov, A.F.; Pal'yanov, Y.N. The morphology of diamond crystals, dissolved in the water containing silicate melts. *Mineral. Zh.* **1990**, *12*, 14–23. (In Russian)
14. Khokhryakov, A.F.; Palyanov, Y.N. Dissolution form of diamond crystals in $CaCO_3$ melt at 7 GPa. *Russ. Geol. Geophys.* **2000**, *41*, 682–687.
15. Khokhryakov, A.F.; Palyanov, Y.N. The evolution of diamond morphology in the process of dissolution: Experimental data. *Am. Mineral.* **2007**, *92*, 909–917. [CrossRef]
16. Khokhryakov, A.F.; Palyanov, Y.N. Influence of the fluid composition on diamond dissolution forms in carbonate melts. *Am. Mineral.* **2010**, *95*, 1508–1514. [CrossRef]
17. Khokhryakov, A.F.; Palyanov, Y.N. Effect of crystal defects on diamond morphology during dissolution in the mantle. *Am. Mineral.* **2015**, *100*, 1528–1532. [CrossRef]
18. Sokol, A.G.; Khokhryakov, A.F.; Palyanov, Y.N. Composition of primary kimberlite magma: Constraints from melting and diamond dissolution experiments. *Contrib. Mineral. Petrol.* **2015**, *170*, 26. [CrossRef]
19. Khokhryakov, A.F.; Palyanov, Y.N.; Sobolev, N.V. Evolution of crystal morphology of natural diamond in dissolution processes: Experimental date. *Dokl. Earth Sci.* **2001**, *381*, 884–888.
20. Khokhryakov, A.F.; Palyanov, Y.N.; Sobolev, N.V. Crystal morphology as an indicator of redox conditions of natural diamond dissolution at the mantle PT parameters. *Dokl. Earth Sci.* **2002**, *385*, 534–537.
21. Pollanck, H.N.; Chapman, D.S. On the regional variation of head flow, geoterms, and lithospheric thickness. *Tectonophysics* **1977**, *38*, 279–296. [CrossRef]

22. Kennedy, C.J.; Kennedy, G.C. The equilibrium boundary between graphite and diamond. *J. Geophys. Res.* **1976**, *81*, 2467–2470. [CrossRef]
23. Khokhryakov, A.F.; Kruk, A.N.; Sokol, A.G. The effect of oxygen fugacity on diamond resorption in ascending kimberlite melt. *Lithos* **2021**, *394–395*, 106166. [CrossRef]
24. Ballhaus, C.; Berry, R.F.; Green, D.H. High pressure experimental calibration of the olivine-orthopyroxene-spinel oxygen geobarometer: Implications for the oxidation state of the upper mantle. *Contrib. Mineral. Petrol.* **1991**, *107*, 27–40. [CrossRef]
25. Campbell, A.J.; Danielson, L.; Righter, K.; Seagle, C.T.; Wang, Y.; Prakapenka, V.B. Pressure–Volume–Temperature Studies of Metal–Oxide Pairs. Available online: https://www.geol.umd.edu/~{}ajc/Posters/CampbellCOMPRES2007poster.pdf (accessed on 23 January 2022).
26. Foley, S.F. A reappraisal of redox melting in the Earth's mantle as a function of tectonic setting and time. *J. Petrol.* **2011**, *52*, 1363–1391. [CrossRef]
27. Kadik, A.A.; Lukanin, O.A. *Degassing of the Upper Mantle upon Melting*; Nauka PH: Moscow, Russian, 1986; 120p. (In Russian)
28. Frost, D.J.; Wood, B.J. Experimental measurements of the fugacity of CO_2 and graphite/diamond stability from 35 to 77 kbar at 925 to 1650 °C. *Geochim. Cosmochim. Acta* **1997**, *61*, 1565–1574. [CrossRef]
29. Bataleva, Y.V.; Palyanov, Y.N.; Sokol, A.G.; Borzdov, Y.M.; Palyanova, G.A. Conditions for the origin of oxidized carbonate–silicate melts: Implications for mantle metasomatism and diamond formation. *Lithos* **2012**, *128–131*, 113–125. [CrossRef]
30. Grassi, D.; Schmidt, M.W. Melting of carbonated pelites at 8–13 GPa: Generating K-rich carbonatites for mantle metasomatism. *Contrib. Mineral. Petrol.* **2011**, *162*, 169–191. [CrossRef]
31. Sokol, A.G.; Kupriyanov, I.N.; Palyanov, Y.N.; Kruk, A.N.; Sobolev, N.V. Melting experiments on the Udachnaya kimberlite at 6.3–7.5 GPa: Implications for the role of H2O in magma generation and formation of hydrous olivine. *Geochim. Cosmochim. Acta* **2013**, *101*, 133–155.
32. Sokol, A.G.; Pal'yanov, Y.N.; Pal'yanova, G.A.; Tomilenko, A.A. Diamond crystallization in fluid and carbonate-fluid systems under mantle P–T conditions: 1. Fluid composition. *Geochem. Int.* **2004**, *42*, 830–838.
33. Palyanov, Y.N.; Borzdov, Y.M.; Khokhryakov, A.F.; Kupriyanov, I.N.; Sokol, A.G. Effect of nitrogen impurity on diamond crystal growth processes. *Cryst. Growth Des.* **2010**, *10*, 3169–3175. [CrossRef]
34. Day, H. A revised diamond-graphite transition curve. *Am. Mineral.* **2012**, *97*, 52–62. [CrossRef]
35. Sokol, A.G.; Borzdov, Y.M.; Palyanov, Y.N.; Khokhryakov, A.F. High-temperature calibration of a multi-anvil high pressure apparatus. *High Press. Res.* **2015**, *35*, 139–147. [CrossRef]
36. Sokol, A.G.; Kruk, A.N.; Chebotarev, D.A.; Palyanov, Y.N. Carbonatite melt–peridotite interaction at 5.5–7.0 GPa: Implications for metasomatism in lithospheric mantle. *Lithos* **2016**, *248–251*, 66–79. [CrossRef]
37. Hernlund, J.; Leinenweber, K.; Locke, D.; Tyburczy, J. A numerical model for steady state temperature distributions in solid-medium high-pressure cell assemblies. *Am. Mineral.* **2006**, *91*, 295–305. [CrossRef]
38. Brey, G.P.; Bulatov, V.K.; Girnis, A.V. Melting of K-rich carbonated peridotite at 6–10 GPa and the stability of K-phases in the upper mantle. *Chem. Geol.* **2011**, *281*, 333–342. [CrossRef]
39. Wyllie, P.J.; Ryabchikov, I.D. Volatile components, magmas, and critical fluids in upwelling mantle. *J. Petrol.* **2000**, *41*, 1195–1206. [CrossRef]
40. Rock, N.M.S. *Lamprophyres*; Blackie: New York, NY, USA, 1991; 284p.
41. Frank, F.C.; Puttic, K.E.; Wilks, E.M. Etch pits and trigons of diamond: I. *Phil. Mag.* **1958**, *3*, 1262–1279. [CrossRef]
42. Orlov, Y.L. *The Mineralogy of Diamond*; John Wiley: New York, NY, USA, 1977; 235p.
43. Fedortchouk, Y.; Canil, D.; Semenets, E. Mechanisms of diamond oxidation and their bearing on the fluid composition in kimberlite magmas. *Am. Mineral.* **2007**, *92*, 1200–1212. [CrossRef]
44. Zhang, Z.; Fedortchouk, Y.; Hanley, J.J. Evolution of diamond resorption in a silicic aqueous fluid at 1–3 GPa: Application to kimberlite emplacement and mantle metasomatism. *Lithos* **2015**, *227*, 179–193. [CrossRef]
45. Frank, F.C.; Lang, A.R. Observation by X-ray diffraction on dislocation in a diamond. *Phil. Mag.* **1959**, *4*, 383–386. [CrossRef]
46. van Enckevort, W.J.P.; Seal, M. Stress birefringence microscopy of dislocations in type-Ia natural diamond. *Phil. Mag.* **1988**, *57*, 939–954. [CrossRef]
47. Khokhryakov, A.F.; Palyanov, Y.N. Revealing of dislocations in diamond crystals by the selective etching method. *J. Cryst. Growth* **2006**, *293*, 469–474. [CrossRef]
48. Rudenko, A.P.; Kulakova, I.I.; Shturman, V.L. Oxidation of natural diamond. In *Novye Dannye o Mineralogii SSSR*; Nauka: Moscow, Russian, 1979; Volume 28, pp. 105–125. (In Russian)
49. Skvortsova, V.L.; Shiryaev, A.A.; Fedortchouk, Y. Influence of ions on diamond resorption. *Diam. Relat. Mater.* **2020**, *104*, 107764. [CrossRef]
50. Wyllie, P.J.; Huang, W.-L. Influence of mantle CO_2 in the generation of carbonatites and kimberlites. *Nature* **1975**, *257*, 297–299. [CrossRef]
51. Mysen, B.O. Silicate-COH melt and fluid structure, their physicochemical properties, and partitioning of nominally refractory oxides between melts and fluids. *Lithos* **2012**, *148*, 228–246. [CrossRef]
52. Mysen, B.O. Structure-property relationships of COHN-saturated silicate melt coexisting with COHN fluid: A review of in-situ, high-temperature, high-pressure experiments. *Chem. Geol.* **2013**, *346*, 113–124. [CrossRef]

53. Mysen, B.O. Water-melt interaction in hydrous magmatic systems at high temperature and pressure. *Prog. Earth Planet. Sci.* **2014**, *1*, 4. [CrossRef]
54. Brooker, R.A.; Kohn, S.C.; Holloway, J.R.; McMillan, P.F.; Carroll, M.R. Solubility, speciation and dissolution mechanisms for CO_2 in melts on the $NaAlO_2{}^{-2}$ join. *Geochim. Cosmochim. Acta* **1999**, *63*, 3549–3565. [CrossRef]
55. Eggler, D.H. The effect of CO_2 upon partial melting of peridotite in the system Na_2O–CaO–Al_2O_3–MgO–SiO_2–CO_2 to 35 kb, with an analysis of melting in a peridotite-H_2O–CO_2 system. *Am. J. Sci.* **1978**, *278*, 305–343. [CrossRef]
56. Luth, R.W.; Palyanov, Y.N.; Bureau, H. Experimental petrology applied to natural diamond growth. *Rev. Mineral. Geochem.* **2021**, *87*, *in press*.
57. Creighton, S.; Stachel, T.; Matveev, S.; Höfer, H.; Mc Cammon, C.; Luth, R.W. Oxidation of the Kaapvaal lithospheric mantle driven by metasomatism. *Contrib. Mineral. Petrol.* **2009**, *157*, 491–504. [CrossRef]
58. Woodland, A.B.; Koch, M. Variation in oxygen fugacity with depth in the upper mantle beneath the Kaapvaal Craton, southern Africa. *Earth Planet. Sci. Lett.* **2003**, *214*, 295–310.
59. Becker, M.; Le Roex, A.P. Geochemistry of South African on- and off-craton, group I and group II kimberlites: Petrogenesis and source region evolution. *J. Petrol.* **2006**, *162*, 169–191. [CrossRef]
60. Kogarko, L.N. Alkaline magmatism and enriched mantle reservoirs: Mechanisms, time, and depth of formation. *Geochem. Int.* **2006**, *44*, 3–10. [CrossRef]
61. Bowen, D.C.; Ferraris, R.D.; Palmer, C.E.; Ward, J.D. On the unusual characteristics of the diamonds from Letšent-la-Terai kimberlites, Lesotho. *Lithos* **2009**, *112* (Suppl. S2), 767–774. [CrossRef]
62. Hetman, C.M.; Smith, B.S.; Robey, J.; Nkotsi, T.; Mohapi, M.; Mohapi, T. Letšeng diamond mine, Lesotho: A variant of Kimberley-type pyroclastic kimberlite emplacement. *Mineral. Petrol.* **2018**, *112* (Suppl. S2), S365–S382. [CrossRef]
63. Moore, A.E. Type II diamonds: Flamboyant Megacrysts? *South Afr. J. Geol.* **2009**, *112*, 23–38. [CrossRef]
64. Kozai, Y.; Arima, M. Experimental study on diamond dissolution in kimberlitic and lamproitic melts at 1300–1420 °C and 1 GPa with controlled oxygen partial pressure. *Am. Mineral.* **2005**, *90*, 1759–1766. [CrossRef]
65. Kamenetsky, V.S.; Kamenetsky, M.B.; Weiss, Y.; Navon, O.; Nielsen, T.F.D.; Mernagh, T.P. How unique is the Udachnaya-East kimberlite? Comparison with kimberlites from the Slave Craton (Canada) and SW Greenland. *Lithos* **2009**, *112*, 334–346. [CrossRef]
66. Mitchell, R.H.; Giuliani, A.; O'Brien, H. What is a Kimberlite? Petrology and Mineralogy of Hypabyssal Kimberlites. *Elements* **2019**, *15*, 381–386. [CrossRef]
67. Palyanov, Y.N.; Borzdov, Y.M.; Bataleva, Y.U.V.; Sokol, A.G.; Palyanova, G.A.; Kupriyanov, I.N. Reducing role of sulfides and diamond formation in the Earth's mantle. *Earth Planet. Sci. Lett.* **2007**, *260*, 242–256. [CrossRef]
68. Palyanov, Y.N.; Sokol, A.G.; Khokhryakov, A.F.; Kruk, A.N. Conditions of diamond crystallization in kimberlite melt: Experimental data. *Russ. Geol. Geophys.* **2015**, *36*, 196–210. [CrossRef]
69. Pal'yanov, Y.N.; Sokol, A.G.; Khokhryakov, A.F.; Pal'yanova, G.A.; Borzdov, Y.U.M.; Sobolev, N.V. Diamond and graphite crystallization in COH fluid at PT parameters of the natural diamond formation. *Dokl. Earth Sci.* **2000**, *375*, 1395–1399.